Applied Thermal Engineering 220 (2023) 119705

Contents lists available at ScienceDirect

Applied Thermal Engineering

journal homepage: www.elsevier.com/locate/apthermeng

Research Paper

Simulation of heat and mass transfer process in a flat-plate loop heat pipe and experimental comparison

Zikang Zhang, Haichuan Cui, Shuaicheng Zhao, Runze Zhao, Tong Wu, Zhichun Liu, Wei Liu *

School of Energy and Power Engineering, Huazhong Univearsity of Science and Technology, Wuhan 430074, China

ARTICLE INFO

Keywords:
Loop heat pipe
Flat-plate evaporator
Heat and mass transfer simulation
Volume of fluid method
Vapor leakage

ABSTRACT

A loop heat pipe is a passive heat transfer device with strong robustness, high efficiency, and good performance, and has been widely utilized in numerous thermal control systems. Herein, an intensive study of a flat-plate evaporator LHP from the perspective of experiment and simulation is presented. First, the vapor leakage problem, which was a common issue for most LHP systems, was solved by filling the assembly clearance with epoxy glue, and a flat-plate LHP system was fabricated to verify its operating performance. Test results indicated that the loop stably performed under various working conditions without temperature oscillation. The maximum heat flux was 11.25 W/cm^2 and the minimum thermal resistance was 0.1340 °C/W. The heater surface temperature remained low except during the dry-out state in wick at the maximum heat load condition where a sharp increase was observed, and temperature hysteresis occurred during variable heat load tests owing to the transport lag in long liquid line. Based on the above experiment, an efficient 3-D CFD computational model was built to simulate the heat and mass transfer process in a flat-plate evaporator by the Volume of Fluid method. In addition, the flow regime with two-phase distribution at the scale of the entire evaporator was calculated by considering the structure effect. Boundary conditions were derived from the experiment and the mass flow rate at the evaporator inlet was deduced from the heat leakage effect in liquid line. Calculation results demonstrated that four symmetric vortices developed inside the compensation chamber and generated uneven subcooled liquid infiltration in wick, further leading to a slight offset of high-temperature zone to the evaporator inlet side. Parameter analysis indicated that the ribs conducted 84 % of the heat conduction using thermal paths formed between the heater surface and liquid–vapor interface. The vapor volume percentage in the vapor collector was above 80 %, and increasing the heat load reduced the vapor volume in wick as well as the percentage of heat adsorbed during evaporation. Experimental comparison illustrated that the model exhibited a high accuracy with an error less than 10.29 %.

1. Introduction

With the rapid development of the telecommunications industry and computer technology, the amount of waste heat generated in electronic devices during normal operation continues to increase, giving rise to an urgent need for high-performance thermal control systems. As a two-phase passive cooling system, a loop heat pipe (LHP) possesses the merits of high heat transfer capacity, flexible installation, and low thermal resistance [1]. Recent progress in LHP indicates that it can meet the heat dissipation requirement and improve the stability of thermal control systems, and it has been widely utilized in space satellites [2,3], deep space exploration [4,5], computer servers [6,7], data centers [8], and electric vehicles [9,10], etc.

The LHP comprises an evaporator, a condenser, and two transport lines. The driving force for the circulation of the working fluid is obtained using a porous wick in the evaporator. The subcooled liquid in wick vaporizes after absorbing heat from the heat source and flows to the condenser through the vapor line. The vapor then condenses into subcooled liquid after dissipating the heat to the condenser and flows back to the evaporator. The wick divides the evaporator into a compensation chamber and vapor collector, and ensures the separation between these two for the proper operation of the capillary transmission.

According to numerous experimental studies, evaporators in LHPs can be classified into two types: cylinder, and flat plate/disk. Wu et al. [11] investigated the effects of pore size and mixing ratio of polymer PMMA in biporous wick to enhance the cylindrical LHP performance.

* Corresponding author.
E-mail address: w_liu@hust.edu.cn (W. Liu).

https://doi.org/10.1016/j.applthermaleng.2022.119705
Received 23 May 2022; Received in revised form 8 November 2022; Accepted 20 November 2022
Available online 25 November 2022
1359-4311/© 2022 Elsevier Ltd. All rights reserved.

Nomenclature

$C1$	viscous resistance factor [m^{-2}]
$C2$	inertial resistance factor [m^{-1}]
c_p	specific heat [J kg^{-1} K^{-1}]
$coeff$	inverse of the relaxation time [s^{-1}]
D	diameter [m]
d_b	diameter of the bubble [m]
d_p	average diameter of the pore inside the wick [m]
E	specific energy [J kg^{-1}]
F_{vol}	source term of the volume force [kg m^{-2} s^{-2}]
g	gravity [N kg^{-1}]
h_{fg}	latent heat of vaporization [J kg^{-1}]
k	thermal conductivity [W/m K^{-1}]
K_p	effective permeability [m^2]
L_{iquid}	liquid line length [m]
m	mass flow rate [kg/s]
M	relative molecule mass [1]
p	pressure [Pa]
Q	heat load at heater surface [W]
$Q_{Amb\text{-}L}$	heat leakage between ambient and liquid line [W]
$Q_{HS\text{-}L}$	background heat leakage between heater surface and liquid line [W]
R	thermal resistance [°C/W]
R_g	universal gas constant [J/mol K^{-1}]
$S_{M,i}$	i th momentum source term [pa m^{-1}]
$S_{m,l}$	liquid source term [kg m^{-3} s^{-1}]
$S_{m,v}$	vapor source term [kg m^{-3} s^{-1}]
S_q	energy source term [W/m^{-3}(−|-)]
t	time [s]
T	temperature [K]
$\boldsymbol{u}$	velocity vector [m/s]
v	velocity [m/s]
$\|v\|$	magnitude of the velocity [m/s]

Greek symbol

α	volume fraction
ε	error [%]
κ	interphase curvature [m^{-1}]
μ	dynamic viscosity [N s/m^{-2}(−|-)]
ρ	density [kg m^{-3}]
σ	coefficient of surface tension [N/m]
φ	porosity of the wick [%]

Subscripts

A	thermal insulation material
Amb	ambient
cal	calculation
Cond	condenser
d1	inner of the liquid line
d2	outer of the liquid line
d3	outer of the thermal insulation material
evap	evaporator
exp	experiment
f1	fluid 1 at inlet
f2	fluid 2 at outlet
l	liquid
LHP	loop heat pipe
i	i th phase (liquid, vapor)
s	solid domain
sat	saturation
sink	heat sink
v	vapor
w	wall of the liquid tube
w1	wall 1 at inlet
w2	wall 2 at outlet
wick	capillary wick

Abbreviations

Amb	ambient
CC	compensation chamber
CFD	computational fluid dynamics
Comp-wall	compensation chamber wall
Cond-in	condenser inlet
Cond-out	condenser outlet
Evap-in	evaporator inlet
Evap-out	evaporator outlet
HS	heater surface
LHP	loop heat pipe
S	evaporator shell
SS304	stainless steel 304
TC	thermocouple
VC	vapor collector
VOF	volume of fluid method
W	wick

Gunnasegaran et al. [12] adopted an Al_2O_3-H_2O nanofluid as the working medium and the cylindrical LHP stabilized faster at a lower wall temperature. Maydanik et al. [13] conducted two comparative tests of ammonia LHP with cylindrical and flat disk evaporators. They pointed out that the LHP with a cylindrical evaporator was less sensitive to internal and external pressures, whereas the LHP with a flat one was lighter and more compact. Additionally, the flat evaporator could directly attach to the electronic chip without excessive installation space and exhibited a strongly isothermal surface temperature, thereby making it a better adaption for practical electronic devices than a cylindrical one. Singh et al. [14] incorporated a biporous copper wick into a miniature LHP and obtained a better evaporative heat transfer than the monoporous wick. Wang et al. [15] employed laser ablation to synthesize two different types of micro- and nanoscale hybrid structures on a boiling pool substrate to enhance the maximum heat flux. Fukushima et al. [16] fabricated a flat plate micro-LHP with a porous polytetrafluoroethylene wick and observed good agreement between the mathematical results. Weisenseel et al. [17] tested biomorphous silicon carbide as a novel wick material in a flat evaporator LHP and the thermal resistance was reduced to 0.3792 °C/W. Both types of aforementioned evaporators should solve a common problem in the manufacturing process, i.e., vapor leakage between the vapor collector and compensation chamber. Failure to completely address this problem deteriorates the capillary capacity of the wick and ultimately the thermal performance of the entire system. Huang et al. [18] proposed a low-cost manufacturing method to create a tight seal and contact of the wick for cylindrical evaporators and the leakage was restrained. For the flat evaporators, He et al. [19] fabricated an evaporator by pouring the wick inside to eliminate the assembling clearance between the wick and evaporator shell. Furst et al. [20] developed a novel additively manufactured evaporator by sintering a wick on an evaporator using the direct metal laser sintering technology. The vapor channels inside the wick ensured that no gap existed between the compensation chamber and the vapor channels. Once the leakage problem is solved by multiple aforementioned methods, the flat-plate evaporator will exhibit superior performance than the cylindrical evaporator, especially for electronic chip heat dissipation scenarios, therefore, extensive research is needed in this regard.

Another aspect that requires attention is the numerical calculation of the LHP components and systems. Research on LHP has mainly focused on experimentation and testing because of their intuitive and highly accurate results. However, owing to the limited selection of materials, long fabrication, and investigation cycles, the experimental results present lengthy feedback to subsequent research for improvement, thereby significantly increasing the research duration and difficulty. By using the numerical calculation method, the material parameters and structural features can be flexibly altered, thus, a multitude of numerical simulations can be conducted rapidly for further guidance in LHP performance improvement.

Numerical calculations in LHP can also be classified into two types: global system simulation using a mathematical model or thermal resistance network, heat and mass transfer process simulation in an evaporator and even a LHP system using CFD analysis. Watanabe et al. [21] proposed heat circuit models to investigate the operating characteristics of LHP and compared them with experimental tests. The increase in heat leakage increased both the operating temperature and minimum start-up heat load. Ramasamy et al. [22] constructed a mathematical model to predict the steady-state temperature of a miniature LHP, which was in good agreement with infrared thermography results. Bernagozzi et al. [9] employed a 1-D lumped parameter model to predict the transient behavior of a LHP with a cylindrical evaporator. An extensive parametric analysis indicated the possibility of using such a model for feasibility studies and optimization purposes. Bai et al. [23] parametrically analyzed the startup characteristics of the LHP system using a node network model and demonstrated its reliability for prediction method under various operating conditions. Jung et al. [24] effectively simulated the temperature and pressure of a LHP with a flat evaporator by employing the thin-film theory at the liquid–vapor interface. For another type of numerical calculation method, Nisikawara et al. [25] utilized a 3-D pore network model with a dispersed pore size wick to simulate the heat-transfer characteristics in an evaporator and observed that the applied heat flux was concentrated on the three-phase contact line. Chernysheva et al. [26] conducted a 3-D heat and mass transfer model for a flat evaporator using the EFDLab software package to predict the temperature distribution and velocity field in a flat evaporator. Zhang et al. [27] adopted the VOF method in a 3-D model of the LHP to evaluate the effect of heat leakage from heated surface to compensation chamber and further fabricated an optimized experiment to confirm the improvement. Li et al. [28] developed a practical quasi 3-D numerical model for a square flat evaporator of a LHP, providing insight into the thermal characteristics during steady-state operation. Mottet et al. [29] analyzed the heat and mass transfer in an evaporator unit cell by a mixed pore net-work model and proved that the bidispersed wick prevented evaporator casing overheating. Li et al. [30] used an advanced phase-change LBM method to simulate the pore scale evaporation heat transfer process in a flat evaporator. Five types of patterns were observed on the liquid–vapor interface with an increase in heat flux.

For most numerical calculations, much effort has been focused either on the parametric analysis of the entire system, while ignoring the heat and mass transfer mechanism in the evaporator, or on the heat and mass transfer process of the local evaporator and wick cell unit, while ignoring the effect of the evaporator structure and the two-phase distribution within. In addition, few studies on the heat and mass transfer of the evaporator were compared with the experimental results and subsequently corrected from it, which reduced the simulation accuracy and provide ineffective guidance for further improving experiments. In this study, a flat-plate evaporator loop heat pipe from the perspective of experiment and simulation with the aforementioned issues addressed is presented. First, the vapor leakage problem of flat-plate evaporator was solved using epoxy glue, which was easier and more economical than the other solutions mentioned above; therefore, a high-performance LHP system was fabricated to collect the experimental data. Subsequently, a 3-D CFD computational model based on the experimental structure was constructed to reveal the heat and mass transfer mechanism inside the evaporator using the volume-of-fluid method. Benefits of this model were that the evaporator structure effect was fully considered, the flow regime and two-phase distribution were calculated at the scale of the entire evaporator, and the model accuracy was verified by comparing the results of simulation and experiment. Boundary conditions were derived from the experimental results and the mass flow rate was deduced using the heat leakage effect in the liquid line. Simulation results indicated that the liquid–vapor interface, temperature distributions, and flow pattern could be well exhibited, and the evaporator working mechanism could be clearly reflected compared to other simulation models. In addition, this model had a good reconstruction of the flat-plate evaporator and fit well with the experimental results in the heater surface and vapor temperatures. Numerous experimental attempts could be saved and improved evaporator structure design and wick property parameters could be obtained before experimental verification. This would be conducive for the structural and design parameter optimization in future work.

2. Experimental setup

2.1. LHP design

The LHP system fabricated in this study consisted of a flat-plate evaporator, a condenser, and two transport lines. The configuration of the flat-plate evaporator with a square structure is shown in Fig. 1. The porous wick sintered from nickel powders with mixed pore formers separated the evaporator into the compensation chamber and vapor collector, thereby impeding the vapor from entering the compensation chamber and inducing the capillary force failure. Due to the complex assembly of the square wick than the flat disk one, the vapor leakage problem was more severe, and thus a two-component epoxy resin adhesive was further adopted on the wick edges to resolve this issue. The outer dimensions of the evaporator were 50.6 × 50.6 × 21.73 mm and the evaporator material was chosen to be SS304 to enhance the pressure-bearing capacity. The wick was square in shape (edge length 39.76 mm and thickness 3.72 mm) and eleven ribs (width 1.9 mm and depth 1.8 mm) were sintered on the wick surface contacting the heater surface to enlarge the liquid–vapor interface. The wick porosity was 74.94 % as measured by Archimedes Method, and the minimum pore diameter was approximately 2.8 μm as derived from the nickel powder diameter. The working media was anhydrous ammonia with a purity of 99.995 %. As a result of the high operating pressure developed by ammonia, the evaporator was sealed by laser welding for better pressure-bearing capacity. Vapor channels and vapor collector were formed between the wick and the heater surface cover, and the vapor channels were set parallel to the vapor line to reduce the vapor flow resistance. A tube-in-tube condenser with a 950 mm length was employed to cool the working medium within the system. The vapor line and liquid line with lengths of 784.5 mm and 786 mm, respectively, connected the evaporator to the condenser. Fig. 2 presents the experimental diagram of the system, and Table 1 lists the main structural parameters of the system components.

2.2. Test methods

The test schematic comprised three parts: heating, cooling, and temperature measuring modules. The heating module was fabricated using a square copper block embedded with four cartridge heaters, and the heat load was regulated and monitored by a voltage regulator and a wattmeter with a 0.5 % accuracy. The active heater surface of the heat block was 16 cm^2. The outer tube of the condenser was cooled by a 50 % glycol solution circulated by a recirculation chiller (BiLon, temperature control accuracy ± 0.5 °C). The gravity effect was eliminated for the evaporator and condenser were placed at the same level. Eleven *T*-type thermocouples with an accuracy of ± 0.5 °C were attached to different positions of the system for temperature measurements, and the temperature signals were processed and collected using a data acquisition

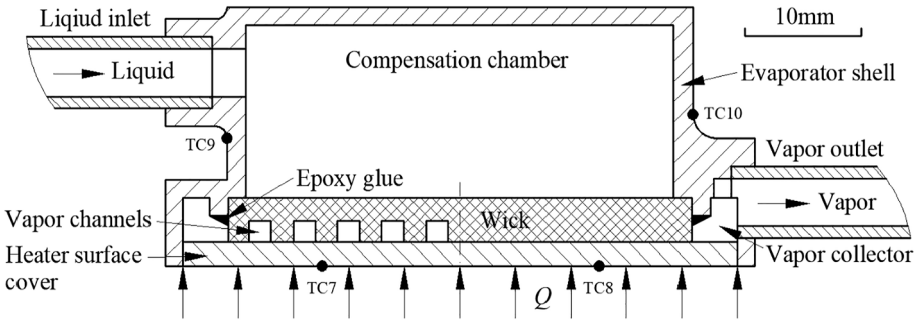

Fig. 1. The cross section of the flat-plate evaporator in square structure.

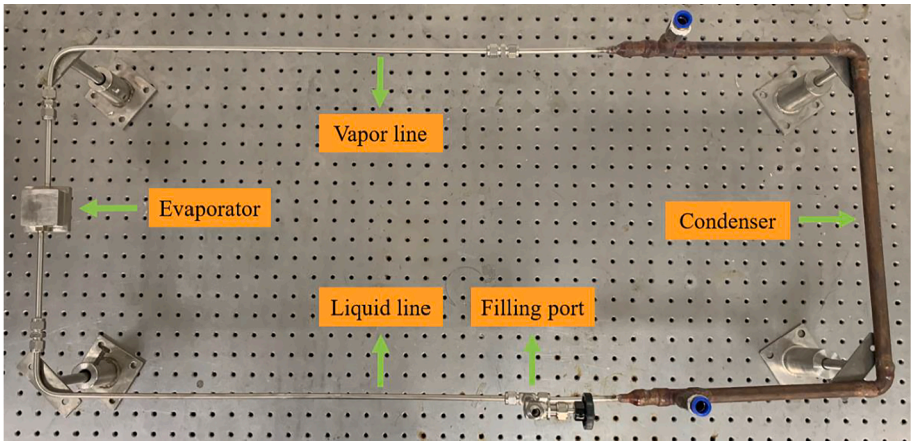

Fig. 2. The experimental diagram of the LHP with flat-plate evaporator.

Table 1
The structural parameters of the components.

The Components	Specification	Dimension/Material
Evaporator	Length/Width/Height	50.6/50.6/21.73 mm
	Material	SS304
Compensation chamber	Length/Width/Height	48/48/14.51 mm
Porous wick	Length/Width/Thickness	39.76/39.76/3.72 mm
	Porosity	74.94 %
	Material	Sintered nickel powders
Vapor line	O. D./I. D./Length	6/4/784.5 mm
	Material	SS304
Liquid line	O. D./I. D./Length	6/4/786 mm
	Material	SS304
Condenser	Inner tube O. D./I. D./Length	6/4/950 mm
	Outer tube O. D./I. D.	16/12 mm
	Inner tube/Outer tube Material	SS304/Copper

system "Keithley 2700" connected to a personal computer. To reduce the heat leakage of the system to the ambient and increase the accuracy of measuring temperature, a 10 mm thick thermal insulation material (PVC/NBR, Fuerda, thermal conductivity 0.034 W/m·K) was employed for system insulation. Prior to charging the working fluid, the loop was evacuated to a pressure of 3.0×10^{-4} Pa to reduce the detrimental effect of non-condensable gas. The charge ratio was set to 74.0 % of the total system volume by calculating the proper liquid–vapor distribution of the system during normal operation. In addition, the saturation pressure of ammonia increased rapidly as the temperature rose, presenting great challenges to the pressure-bearing capacity of the system. Thus, the vapor temperature was maintained below 40 °C for experimental safety, and the heater surface temperature was maintained below 70 ± 2 °C to satisfy the heat dissipation requirements of most electronic devices. The test schematic of the flat plate LHP system is shown in Fig. 3 with thermocouple positions indicated by TCs.

3. Experimental results

3.1. Start-up tests

The start-up process reflects the thermal characteristics of the system in a realistic electronic cooling scenario. Fig. 4 presents the start-up processes at 4 different heat load conditions from low to high with a heat sink temperature of − 10 °C. Once the heat load was applied to the evaporator, the vapor quickly flowed to the condenser after forming inside the wick, and the heater surface and condenser inlet temperatures rose rapidly. The residual fluid in the liquid line also advanced by a short distance, leading to a minute decline in evaporator inlet temperature. When the loop reached the steady state, a temperature difference always existed between the condenser outlet and the evaporator inlet owing to the heat leak effect between the liquid line and the ambient. Furthermore, this temperature difference declined as the heat load increased because a higher heat load resulted in a higher mass flow rate within the loop and restrained the heat leak effect. This improvement in solving the vapor leakage problem is evident in Fig. 4 (c) and (d). Following the fill of assembly clearance by the epoxy glue, no vapor penetrated the compensation chamber even at considerably high heat loads, thereby ensuring that a sufficient subcooled liquid entered the compensation chamber. Hence, the operating pressure inside remained at a low level, and the pressure difference across the wick enlarged. The driving force of the loop was enhanced by maximizing the capillary performance, thereby reducing the heater surface temperature. When the heat load increased from 170 W to 180 W, the overshoot in heater surface temperature was replaced by a further increase. Numerically speaking, the

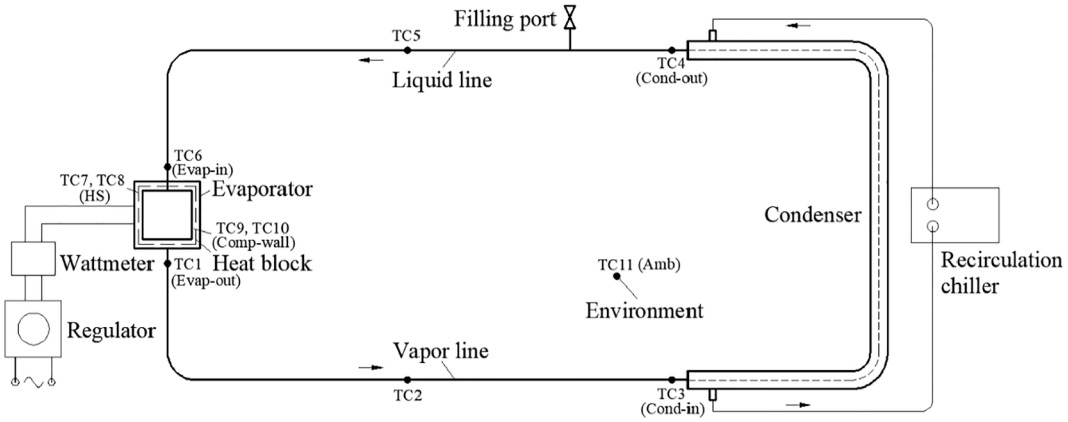

Fig. 3. The test schematic of the LHP with flat-plate evaporator.

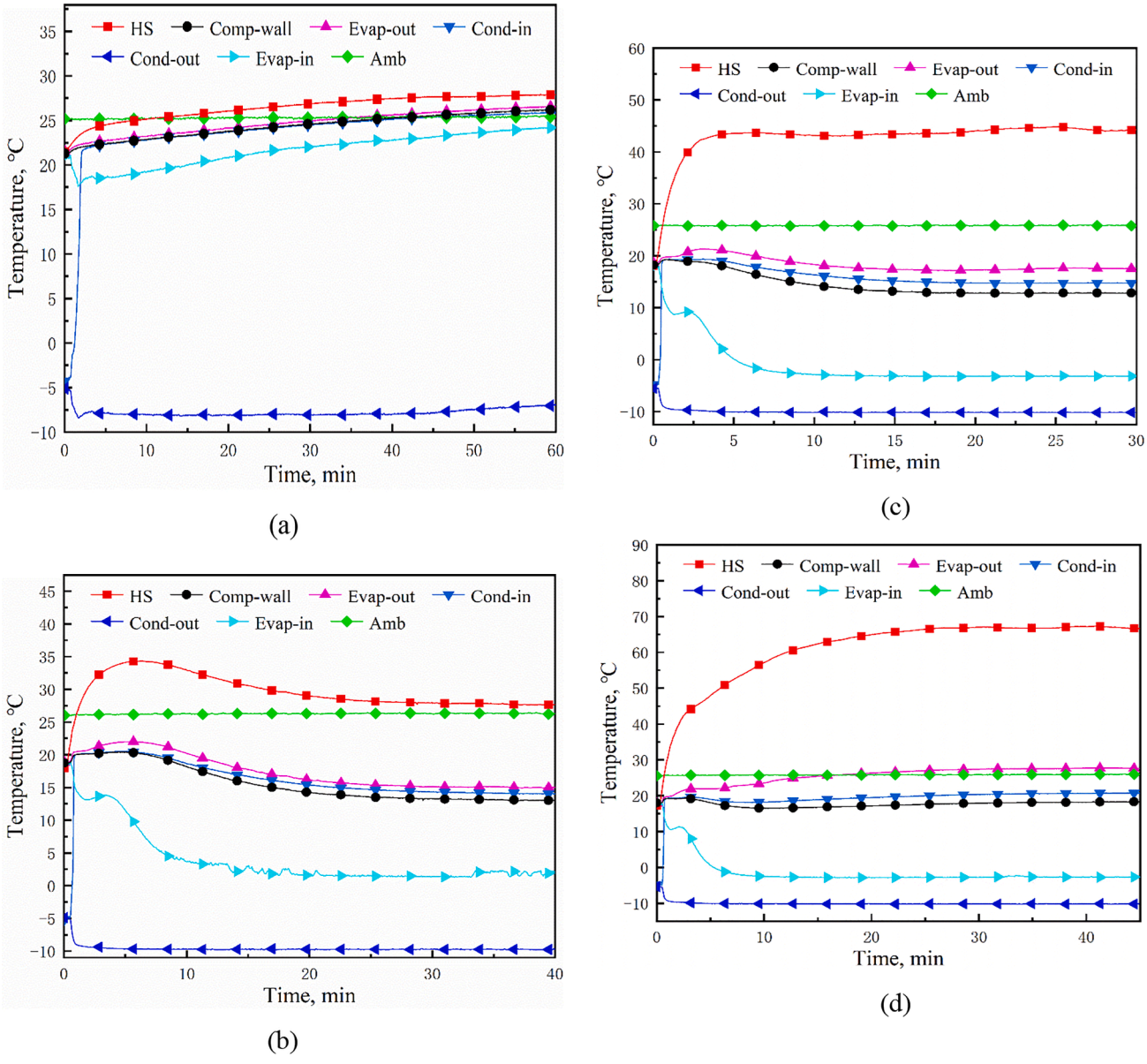

Fig. 4. Start-up processes at T_{sink} = − 10 °C. (a) Q = 10 W. (b) Q = 90 W. (c) Q = 170 W. (d) Q = 180 W.

heater surface temperature rose from 44.33 to 66.97 °C. Since the assembly clearance between the wick and shell was blocked by the epoxy glue, vapor leakage from this area was completely eliminated. However, the liquid–vapor interface extended too deep into the wick that a small amount of vapor started entering the compensation chamber. The pressure difference mentioned above was greatly reduced, and the wick suffered a serious decline in capillary performance on account of the formation of a dry-out state inside. A warmer working fluid was provided to the wick and the operating temperature was increased higher. Thus, the operating condition of the loop deteriorated, accounting for a significant augment in heater surface temperature than the previous working situation. Compared with other LHP systems [31,32], the blockage of vapor leakage on the assembly clearance by the epoxy glue in this loop could improve the thermal performance over a wide heat load range except for the maximum heat load condition. Overall, the maximum allowable heat load was 180 W (heat flux 11.25 W/cm^2). No temperature oscillation was observed and the loop reached a stable state with strong reliability and low latency.

3.2. Variable heat load tests

Fig. 5 presents two variable heat load processes at stepwise and random heat load cycles with a heat sink temperature of − 10 °C.

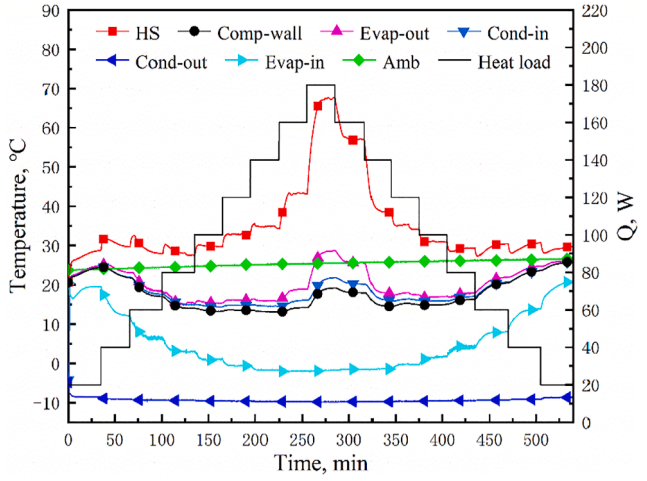

Fig. 5. Variable heat load processes at T_{sink} = − 10 °C. (a) Stepwise heat load cycle. (b) Random heat load cycle.

Apparently, the loop could adjust quickly to different heat load conditions and reach a stable state without any temperature oscillation. On the one hand, when the maximum heat load was applied to the loop, the effect of the vapor leakage problem gradually took on, and the driving force produced by the wick subsequently reduced, indicating that the wick started to suffer a severe dry-out state. Hence, the temperature rise in heater surface was significant regardless of the heat load cycle conditions. As shown in Fig. 5 (a), the heat load started to decline after 280 min and the heater surface temperature subsequently decreased. Whereas the dry-out effect of the wick persisted for a moment, resulting in a relatively high operating pressure in compensation chamber, and the insufficient driving force caused the heater surface temperature to be higher than that in the ascending stage. Only by further reducing the heat load could the wick performance recover from the dry-out effect by supplementing the sufficient subcooled fluid, and could the heater surface temperature be returned to the same level as in the ascending stage. In addition, such dry-out would not affect the temperature distribution of the two stages before and after the high heat load conditions. On the other hand, when the heat load was changed in Fig. 5 (a), the adjustment of the mass flow rate always suffered a certain lag due to the transport hysteresis of the working fluid caused by the long liquid line, that was, in the early period of the ascending stage, the heater surface temperature increased slightly before reducing and stabilizing, and in the later period of the descending stage, it reduced slightly before increasing and stabilizing While the heat load was increased in the ascending stage, the heater surface temperature was first affected and rose, but the adjustments of the subcooled degree and the mass flow rate of the liquid in evaporator inlet were regulated very slowly. As the mass flow rate gradually went up with the heat load, more subcooled liquid entered the evaporator. The wick was better cooled and then the heater surface temperature reduced and stabilized consequently. For the descending stage, the mass flow rate remained high for a short time before decreasing during each heat load alternation, hence, the subcooled liquid was adequate for a short time and the heater surface temperature suffered a sharp reduction before increasing and reaching a steady state. Such a hysteresis phenomenon could also be observed in the random heat load cycle shown in Fig. 5 (b).

3.3. Thermal characteristic analysis

The temperature distribution of the evaporator at different heat loads is illustrated in Fig. 6, where the variation trends of the three heat sink temperatures are almost the same. As the heat load rose, the heater

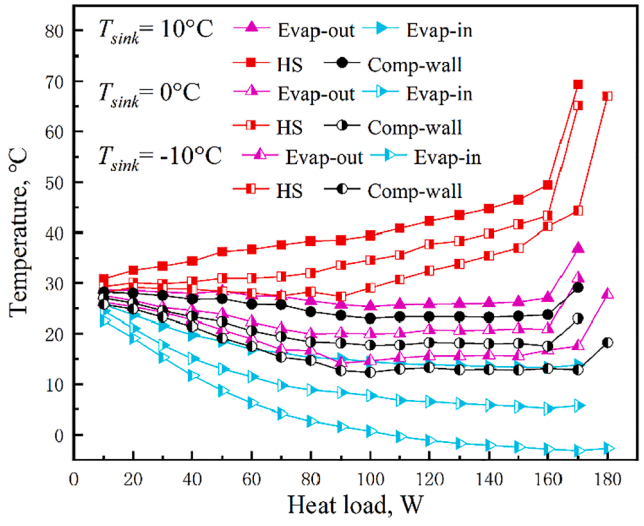

Fig. 6. Temperature distribution of the evaporator at different heat sink temperatures and different heat loads.

surface temperature started to increase, more vapor was produced from the wick and the mass flow rate increased by degrees. Therewith, the heat leak of the backflow liquid gained from the ambient was reduced, leading to a gradual decrease in the evaporator inlet temperature as well as the compensation chamber temperature. More subcooled liquid was supplied to the wick, and the vapor temperature dropped slightly. When the driving force generated by the wick reached its maximum, the rapid backflow of the subcooled liquid in liquid line made the ambient heat leak effect no longer intensified, and the evaporator inlet, compensation chamber, and vapor temperatures started to stabilize. The heater surface, except for the condition of the heat sink temperature of − 10 °C, maintained a nearly uniform rise speed. However, for the heat sink temperature of − 10 °C, the subcooled degree of the backflow liquid returning to the evaporator and evaporation was sufficient such that the heater surface temperature even dropped slightly. Only when the applied heat load was higher than 90 W and restrained the ambient heat leak effect did the heater surface temperature come to rise slightly. For the maximum heat load condition, vapor from the vapor collector penetrated the compensation chamber and its operating pressure and temperature increased simultaneously. Less subcooled liquid was supplied to the wick and the vapor temperature rose as well. These all resulted in a rapid increase in heater surface temperature, which even approached the limit temperature of electronic devices.

By calculating the evaporator thermal resistance, the evaporator heat transfer capacity can be evaluated numerically. The defined calculation can be written as,

$$R_{evap} = \frac{T_{HS} - T_{Evap-out}}{Q} \tag{1}$$

Fig. 7 illustrates the evaporator thermal resistance versus heat load at different heat sink temperatures. The evaporator thermal resistance first dropped rapidly and then rose slightly before reducing and reaching a minimum value. As the heat load increased from a low value, a higher evaporation intensity was acquired and the liquid–vapor interface started to expand inside the vapor channel, resulting in a sudden descent in the evaporator thermal resistance. For the medium heat load range, the vapor collector was filled with the vapor phase, and the liquid–vapor started to enter the wick interior. During this transition stage, the effect of the heat load rise was more pronounced than that of the improvement caused by the liquid–vapor interface enlargement, hence, a small augment was observed in the evaporator thermal resistance. Further increasing the heat load could reduce the evaporator thermal resistance to a certain degree for the liquid–vapor interface was enlarged and penetrated the wick interior. However, when the heat load was close to the maximum value, a small amount of vapor penetrated the compensation chamber across the wick, reducing the capillary force and forcing the wick to turn into a dry-out state. The vapor layer inside the wick became too thick and hindered normal thermal conduction from the heater surface to the liquid–vapor interface, which caused a high reversal increase in the evaporator thermal resistance. Overall, the evaporator thermal resistance was below 0.2137 °C/W, and the minimum value was 0.1340 °C/W at a heat sink temperature of 10 °C and a heat load of 140 W. Higher heat sink temperature ensured a warmer backflow of liquid into the evaporator, the temperature difference between the liquid–vapor interface and heater surface was reduced, and thus the minimum resistance was much lower. Through the error analysis by considering the measurement instrument accuracies, the uncertainty of the evaporator thermal resistance in the experiment ranged between 6.124 and 0.357 %, and the maximum and minimum values were taken at the condition of the heat loads 10 W and 180 W, respectively.

The heat transfer capacity of the entire loop can be evaluated by the LHP thermal resistance, which is defined as,

$$R_{LHP} = \frac{T_{HS} - T_{Cond}}{Q} \tag{2}$$

Fig. 8 illustrates the LHP thermal resistance versus heat load at different heat sink temperatures. Before reaching the maximum heat load condition, as the heat load increased, the evaporator working capacity increased by the enlargement of the liquid–vapor interface and the LHP thermal resistance reduced accordingly. Once the wick suffered a dry-out state at the maximum heat load condition, the deterioration caused by the thick vapor layer led to a reduction in the loop thermal performance, that is, the LHP thermal resistance increased with the evaporator thermal resistance. Furthermore, increasing the heat sink temperature shrank the temperature difference between the evaporator and condenser. The loop worked more efficiently with a lower ambient effect, thereby accounting for the reduction in LHP thermal resistance. The LHP thermal resistance ranged between 1.8470 and 0.2902 °C/W, and the minimum value was achieved at a heat sink temperature of 10 °C and a heat load of 170 W. The uncertainty of the LHP thermal resistance in the experiment ranged between 5.085 and 0.326 %, and the maximum and minimum values were taken at the condition of the heat loads 10 W and 180 W, respectively.

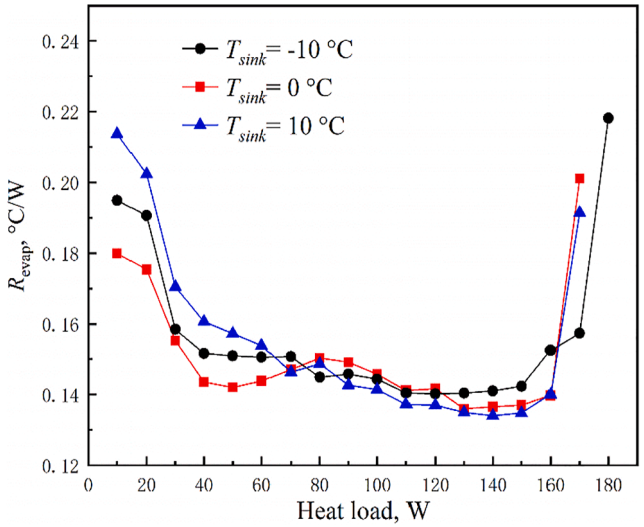

Fig. 7. The evaporator thermal resistances at three heat sink temperatures.

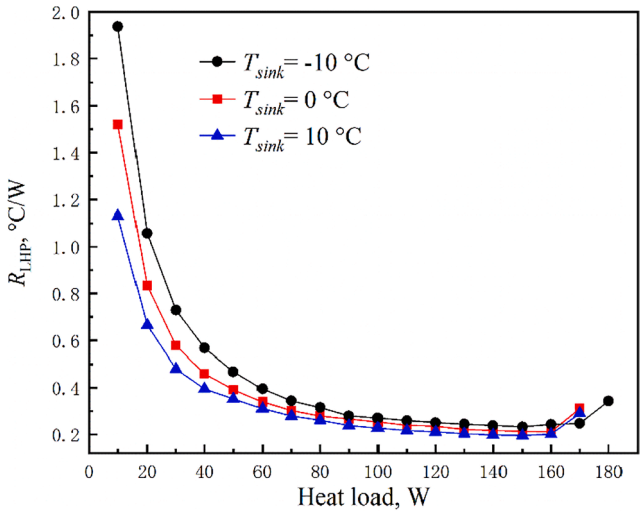

Fig. 8. The LHP thermal resistances at three heat sink temperatures.

4. Simulation model and details

4.1. Model description

By using the Lee model [33] of the volume-of-fluid (VOF) method, the flat-plate evaporator could be numerically analyzed with the heat and mass transfer process thoroughly illustrated. Furthermore, the numerical simulation could be corrected with the experimental results, and a more accurate 3-D CFD computational model of the flat-plate evaporator could be obtained for future optimization studies. Several assumptions are made before introducing the model, including that the working media satisfies the continuous medium hypothesis, the fluid is incompressible, and the liquid and vapor thermophysical properties are considered to be constant.

The continuity, momentum, and energy equations are employed to describe the fluid flow and heat transfer. By considering the liquid and vapor phase volume variations, the mass conservation law can be expressed as [34],

$$\alpha_l + \alpha_v = 1$$

The continuity equations for the vapor and liquid phases can be written as follows [34],

$$\frac{\partial \alpha_l}{\partial t} + \nabla\cdot(u_l\alpha_l) = \frac{S_{m,l}}{\rho_l} \tag{4}$$

$$\frac{\partial \alpha_v}{\partial t} + \nabla\cdot(u_v\alpha_v) = \frac{S_{m,v}}{\rho_v} \tag{5}$$

where $S_{m,l}$ and $S_{m,v}$ represent the fluid evaporation and condensation processes and satisfy. In addition, the source terms can be calculated by comparing the local computational domain temperature with the saturation temperature, through which the evaporation and condensation rates of the working fluid can be numerically determined [33],

$$S_{m,v} = coeff\cdot\alpha_l\rho_l\frac{|T_l - T_{sat}|}{T_{sat}},\ T_l \geqslant T_{sat}(evaporation) \tag{6}$$

$$S_{m,l} = coeff\cdot\alpha_v\rho_v\frac{|T_{sat} - T_v|}{T_{sat}},\ T_v \leqslant T_{sat}(condensation) \tag{7}$$

where *coeff* is defined as [35,36],

$$coeff = \frac{6}{d_b}\sqrt{\frac{M}{2\pi R_g T_{sat}}}h_{fg}\left(\frac{\alpha_v\rho_v}{\rho_l - \rho_v}\right) \tag{8}$$

The momentum conservation equation takes the gravitation, friction, and surface tension into account and can be written as [37],

$$\frac{\partial}{\partial t}(\rho\vec{u}) + \nabla\cdot(\rho\vec{u}\vec{u}) = -\nabla p + \nabla\cdot[\mu(\nabla\vec{u} + \nabla\vec{u}^T)] + \rho\vec{g} + F_{vol} \tag{9}$$

where F_{vol} is deduced by the continuum surface force (CSF) model and can be written as [38],

$$F_{vol} = \sigma\frac{\alpha_l\rho_l\kappa_v\nabla\alpha_v + \alpha_v\rho_v\kappa_l\nabla\alpha_l}{0.5(\rho_l + \rho_l)} \tag{10}$$

The energy conservation equation takes the heat transfer of the phase change into consideration and can be written as [37],

$$\frac{\partial}{\partial t}(\rho E) + \nabla\cdot[\vec{u}(\rho E + p)] = \nabla\cdot[k\nabla T] + S_q \tag{11}$$

where S_q satisfies [34],

$$S_q = -h_{fg}S_{m,l} = h_{fg}S_{m,v} \tag{12}$$

By using the UDF method, the governing equations with the aforementioned source terms can be added to the computational model.

The wick inside the 3-D CFD computational domain is simulated by the porous media model, which is widely used in single phase and multiphase simulation problems. A momentum source term is added to the standard fluid flow equations, and it can be divided into two parts: a viscous loss term, and an inertial loss term [37],

$$S_{M,i} = -\left(C_1\mu v_i + C_2\frac{1}{2}\rho|v_i|v_i\right) \tag{13}$$

The porous wick in the 3-D model is simplified as a mono-porous medium, and by using the Ergun equations, the viscous resistance factor *C1* and inertial resistance factor *C2* can be written as follows [39],

$$\frac{1}{C_1} = \frac{d_p^2}{150}\frac{\varphi^3}{(1-\varphi)^2} \tag{14}$$

$$C_2 = \frac{3.5}{d_p}\frac{1-\varphi}{\varphi^2} \tag{15}$$

Therefore, the calculated viscous resistance coefficients of the liquid and vapor are 1.27×10^{12} m^{-2} and 2.11×10^{15} m^{-2}, and the inertial resistance coefficients of the liquid and vapor are 4.96×10^{5} m^{-1} and 1.62×10^{6} m^{-1}, respectively. The effective permeability was calculated according to Carman-Kozeny formula [40],

$$K_p = \frac{d_p^2\varphi^3}{180(1-\varphi)^2} \tag{16}$$

The energy equation in the solid domain is calculated as [34],

$$\frac{\partial}{\partial x_i}\left(k_s\frac{\partial T}{\partial x_i}\right) = 0 \tag{17}$$

4.2. Model geometry

Fig. 9 presents the perspective computational domain of the flat-plate evaporator of the 3-D CFD simulation model. As in the previous experiment, the wick divided the evaporator into the compensation chamber and vapor collector. Liquid first entered the compensation chamber from the evaporator inlet, then penetrated the wick and turned into vapor before finally flowing out from the vapor channel, vapor collector, and evaporator outlet in succession. The main structural parameters of the wick are presented in Table 2 where all values are the same as those of the system components in the previous experiment. Besides, to simplify the computational domain, the edge chamfers and fillets of the evaporator in the experiment are ignored in the 3-D CFD simulation model, and the evaporator outlet in Fig. 9 is in a cuboid shape with the same hydraulic diameter as the cylindrical evaporator inlet for a better drawing of the computational grid to obtain a higher mesh quality.

4.3. Boundary conditions and solution methods

The boundary conditions of the simulation model include the inlet and outlet options, wall conditions, and working fluid thermophysical properties, which are all derived from the experimental results. The velocity inlet and outflow outlet boundaries are applied to the evaporator inlet and outlet, and the velocity magnitude is derived from the mass flow rate calculation described in the following section by utilizing the heat leakage effect in the liquid line. The inlet temperature is the same as the evaporator inlet temperature in the experiment, and the saturation temperature that controls the evaporation process inside the wick is the average of the compensation chamber and evaporator outlet temperatures for the wick is placed between these two places. For the wall conditions, the outside of the evaporator shell is in the natural convection heat transfer condition with a fixed heat transfer coefficient of 8 W/m^{2}K and the same free stream temperature as the experimental ambient temperature. The wall conditions between the fluid domains are the matching options and between the fluid and solid domains are the coupled wall options. The contact angle of liquid and vapor on wick

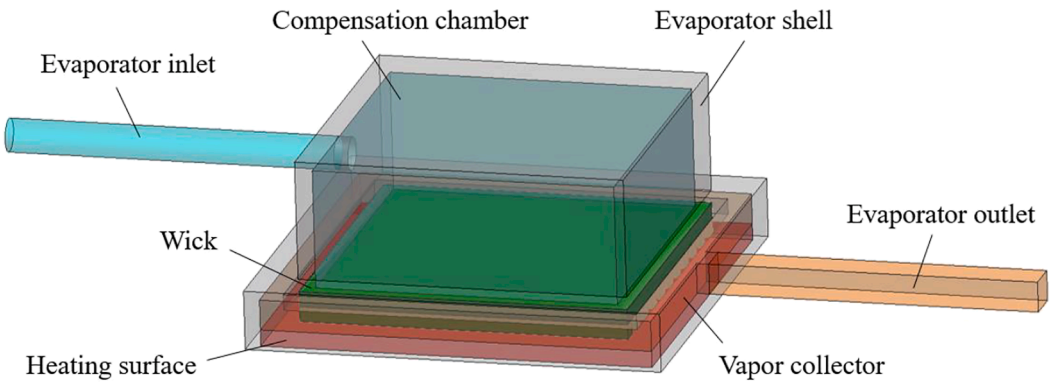

Fig. 9. The computational domain of the flat-plate evaporator.

Table 2
The structural parameters of the computational domain.

The Components	Specification	Dimension/Material
Evaporator shell	Outer length/width/height	50.6/50.6/21.73 mm
	Material	SS304
Compensation chamber	Inner length/width/height	36.7/36.7/14.51 mm
Porous wick	Length/Width/Thickness	39.76/39.76/3.72 mm
	Fin width/depth	1.9/1.8 mm
	Porosity	74.94 %
	Minimum pore diameter	0.0026 mm
	Material	Nickel
Working fluid	Material	Ammonia

surface is assumed to be 50° for the wick has high permeability and the fluid possesses good wettability with the wick. The heat flux is loaded within a range of 40 × 40 mm of the heater surface center while keeping the total value the same as the actual heat load in the experiment. Other locations are set as adiabatic conditions. With reference to the NIST software, the thermophysical parameters of the liquid and vapor are determined by the saturated states of the evaporator inlet temperature and saturation temperature, respectively, and the latent heat value of the evaporation and condensation is obtained from the saturation temperature. In addition, the heat transfer in the solid domain is calculated using Fourier's law of heat conduction.

Due to the low flow velocity of liquid, the viscous model inside the wick is considered to be a laminar flow, and the heat transfer model between the wick and fluid is in thermal equilibrium. The thermophysical properties of the wick, including the effective thermal conductivity, density, and specific heat capacity, are calculated by the weight average method that takes the porosity into account,

$$k_{wick} = \varphi k_l + (1-\varphi)k_s \tag{18}$$

$$\rho_{wick} = \varphi \rho_l + (1-\varphi)\rho_s \tag{19}$$

$$c_{p,wick} = \varphi c_{p,l} + (1-\varphi)c_{p,s} \tag{20}$$

The computational domain grid is generated by ICEM CFD 2019 *R*3 and the numerical calculation was performed by ANSYS Fluent 2019 *R*3. The mathematical model adopts the steady solution with the VOF method solved by the implicit formulation, and with the body force formulation solved by the implicit format for faster calculation. The primary phase is liquid and the second phase is vapor. The turbulent model is in the SST *k-w* format and the calculation solver is the pressure-based type. The Coupled algorithm is adopted for pressure–velocity coupling, QUICK for momentum and energy, PRESTO for pressure, Compressive for volume fraction, and First Order Upwind for the remaining period. By using the Piecewise Linear Interface Calculation (PLIC), the interface of the vapor phase can be specifically determined and constructed. The calculation is considered converged when the residuals are less than 10^{-4} and the vapor volume ratios for each fluid domain reach stabilization.

Fig. 10 depicts the computational domain and mesh of the flat-plate evaporator. The model is divided into different parts and each grid of parts is constructed by block before coupling together. Both the solid and fluid domains are meshed with a cartesian hexahedral grid to maintain high grid quality for calculation. The total number of elements and nodes are 1,393,776 and 1237562, respectively, and the solid–fluid contact surface adopts coupled interface. Ogrid is also used for the cylindrical inlet of compensation chamber to achieve a high quality mesh. In the mesh independence study, by changing the maximum grid size, the verification was performed using three sets of grids with element numbers of 645420, 1237562, and 2,596,039 for calculation, and the simulation results were compared with the experimental results, respectively. Table 3 listed the detailed error values of heater surface and evaporator outlet temperatures at a heat load of 120 W. Temperature errors of heater surface for each group were 7.78, 4.23, and 5.78 %, and temperature errors of evaporator outlet were 8.40, 8.40, and 8.36 %, respectively. The minimum error of the heater surface temperature

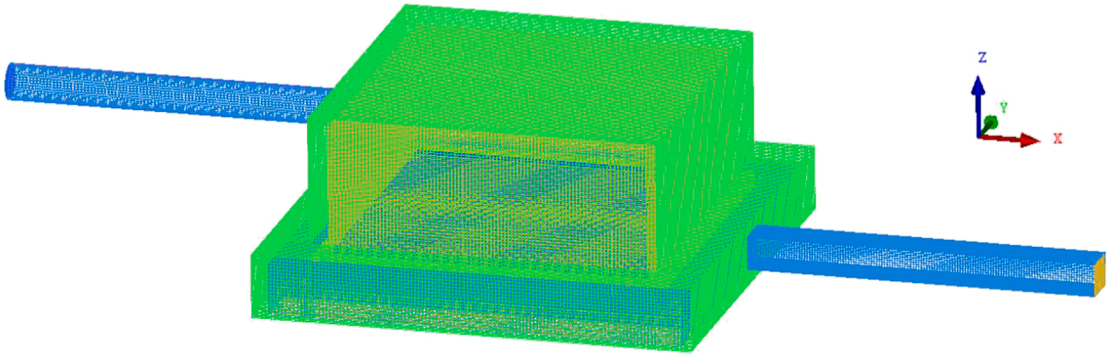

Fig. 10. The overall grids of the flat-plate evaporator.

Table 3
The mesh independency verification at different grid numbers.

Grid element number	Heater surface temperature			Evaporator outlet temperature		
	Simulation (K)	Experiment (K)	Error (%)	Simulation (K)	Experiment (K)	Error (%)
645,420	313.347	310.913	7.78 %	292.713	293.913	8.40 %
1,237,562	312.237	310.913	4.23 %	292.713	293.913	8.40 %
2,596,039	312.721	310.913	5.78 %	292.718	293.913	8.36 %

was achieved at element number of 1237562, and the evaporator outlet temperatures for the three groups remained nearly unchanged. In order to accelerate the computation while maintaining computational precision, a grid of 1,237,562 elements was chosen for the subsequent calculation.

4.4. Mass flow rate calculation

As illustrated in Fig. 4, the temperature difference between the condenser outlet and evaporator inlet caused by the ambient heat leak effect always exists and is altered by the heat load range. This discrepancy is caused by the heat leakage effect between the ambient and liquid line. The mass flow rate inside the liquid line is small, and the subcooled liquid from the condenser is still susceptible to the ambient while flowing through the liquid line even when a thick thermal insulation material was wrapped. Hence, by utilizing the heat leakage effect in the liquid line, the mass flow rate of the loop could be deduced from the experimental results. Fig. 11 illustrates the simplified calculation model of the heat leakage inside the liquid line. TC4, TC 5, and TC6 are placed at the condenser outlet, middle of the liquid line, and evaporator inlet, respectively. TC 4 measures the temperature of the backflow fluid from the condenser and is the same as the condenser temperature (heat sink temperature). TC 5 is affected by the ambient heat leakage effect ($Q_{Amb\text{-}L}$). As for TC6, it is not only affected by the ambient heat leakage effect, but also by the background heat conduction of the evaporator ($Q_{HS\text{-}L}$). However, determining the $Q_{HS\text{-}L}$ value is difficult for the structure of the evaporator shell is complex. By using the steady state heat conduction model of a cylinder wall in Fig. 12, $Q_{Amb\text{-}L}$ is much more predictable, and therefore, the temperature rise between TC4 and TC5 is adopted to derive the mass flow rate of the working fluid in this system.

The $Q_{Amb\text{-}L}$ in Fig. 12 refers to the amount of heat leakage from the ambient between the inlet and outlet. The outer surface temperature of insulation material is assumed to be equal to the ambient temperature T_{Amb}. Thus, $Q_{Amb\text{-}L}$ can be written as,

$$Q_{Amb-L} = \frac{2\pi L_{liquid}\left(\frac{T_{f1}+T_{f2}}{2} - T_{Amb}\right)}{\ln(D_{d2}/D_{d1})/\lambda_w + \ln(D_{d3}/D_{d2})/\lambda_A} \tag{21}$$

Heat leakage between the ambient and liquid line leads to an increase in the sensible heat of the fluid inside the tube. Thus, $Q_{Amb\text{-}L}$ can also be written as,

$$Q_{Amb-L} = mc_{p,l}(T_{f2} - T_{f1}) \tag{22}$$

The thermophysical properties of the fluid are determined with reference to the average inner fluid temperatures T_{f1} and T_{f2}. Since the experiment cannot directly measure the inner fluid of the liquid line, and meanwhile the thermal conductance of the liquid tube made of SS304 is much larger than that of the insulation material, the inner fluid

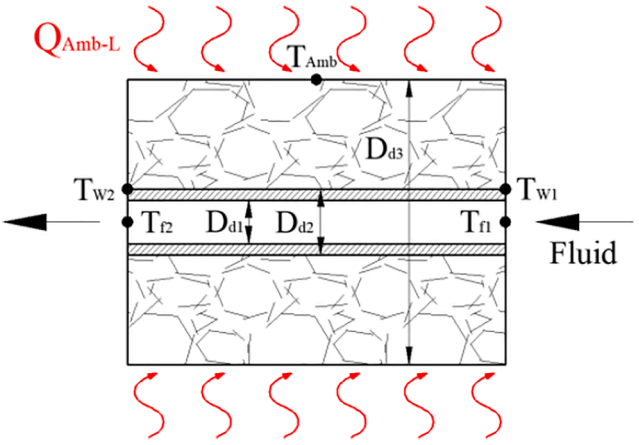

Fig. 12. The model of steady state heat conduction through a cylinder wall.

temperatures T_{f1} and T_{f2} can be assumed to be equivalent to the measuring point temperatures T_{w1} and T_{w2} on the tube wall in Eq. (20) and (21), respectively. By solving the above two equations simultaneously, the mass flow rate of LHP m can be derived, and the velocity magnitude of the evaporator inlet can be determined for subsequent

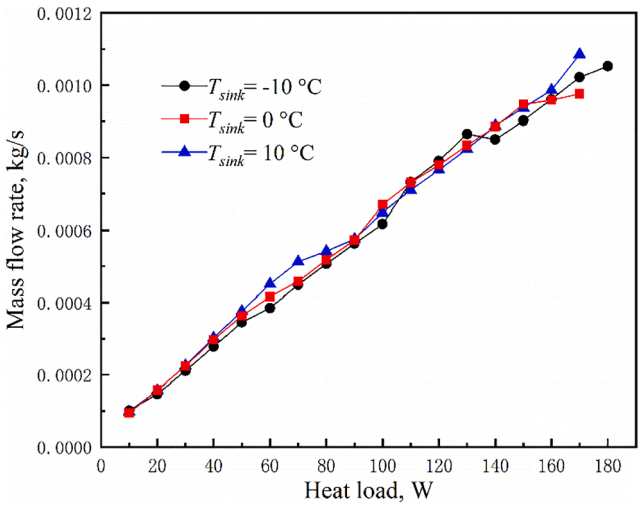

Fig. 13. The mass flow rate of the loop versus heat sink temperature and heat load.

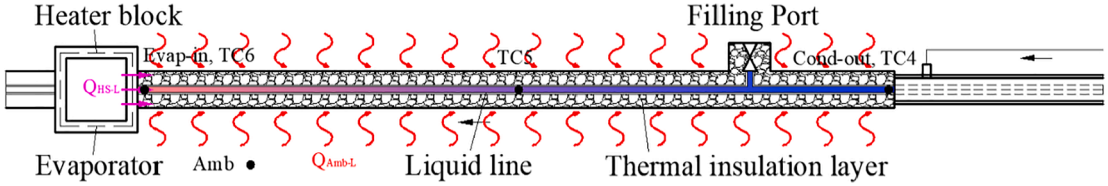

Fig. 11. The simplified calculation model of determining the mass flow rate.

calculations. Furthermore, the theoretical tube wall temperatures T_{w1} and T_{w2} are recalculated using the steady state heat conduction formula of the cylinder wall and compared with the experimental measurement point temperatures. The discrepancy is less than 0.0001 K and the equivalent assumption above is reasonable.

Fig. 13 presents the mass flow rate calculated above against heat load and heat sink temperature. The mass flow rate was essentially linearly proportional to the heat load. A higher heat load enlarged the evaporation interface and capillary force inside the wick, thereby increasing the mass flow rate. For the circumstance of the same heat load condition, the mass flow rates of three heat sink temperatures were nearly the same, and the maximum discrepancy between each other was less than 17.0 %. This indicated that the wick capillary performance was independent of the heat sink temperature. The evaporator performance was affected by the heat sink temperature in Fig. 6 just because of the alternation of the liquid subcooled degree in evaporator inlet. The maximum mass flow rate was 0.001086 kg/s and was achieved at a heat sink temperature of 10 °C and heat load of 170 W, and the minimum mass flow rate was 9.45×10^{-5} kg/s and was achieved at a heat sink temperature of 0 °C and heat load of 10 W.

5. Calculation results

5.1. Flow regime analysis

The streamline diagram and the vapor phase distribution with the area of the vapor volume above 50 % marked at a heat load of 120 W and heat sink temperature of 0 °C are presented in Fig. 14. The subcooled fluid from the evaporator inlet first scoured the furthest wick surface at the evaporator outlet side under the gravity effect and was then reflected by the restriction of the compensation chamber wall, forming two symmetric vortices. A portion of the fluid penetrated the wick while passing by its surface and flowed back to the evaporator inlet side, where it was reflected again by the compensation chamber wall, forming another two symmetric vortices. While the subcooled liquid turned into vapor after crossing the wick, the large discrepancy between the densities of the two phases led to a significant increase in the flow velocity in the vapor channels, and owing to the convergence effect of the vapor collector and the reduction of the flow cross section, the velocity at the evaporator outlet became much larger. The vapor distribution indicated that nearly all the vapor was concentrated at the lower part of the wick, vapor channels, vapor collector, and evaporator outlet, and no vapor phase was observed inside the compensation chamber as a result of the large flow resistance in wick. This proved that such a distribution confirmed the actual situation during normal LHP operation.

5.2. Temperature, velocity, and phase distributions

The temperature and vapor phase distributions of the flat-plate evaporator at the X and Y direction cross sections are illustrated in Fig. 15. The streamline track of the fluid is marked by the direction of the velocity. As shown in the Y-direction central cross sections at the rib area in Fig. 15 (a) and (b), the subcooled fluid first scoured the compensation chamber wall and wick surface at the evaporator outlet side, taking away the heat leakage here, then flowed to the evaporator inlet side and penetrated the wick with a lower subcooled degree. Hence, the wick was in a state of unequal wetting by the different temperatures of working fluid, further leading to an uneven distribution of the evaporation interface, that is, the liquid–vapor interface on the left side was more infiltrated into the wick than on the right side. For the Y-direction cross section at vapor channel area in Fig. 15 (c) and (d), the temperature and vapor phase distributions showed the same pattern in Fig. 15 (a) and (b). Once the subcooled liquid entered the wick, the fluid maintained a vertical downward flow trend and moved rapidly toward the evaporator outlet after converging in the vapor channels. From the X-direction central cross sections in Fig. 15 (e) and (f), two symmetric vortices could be distinctly observed at the upper side of the compensation chamber. Through these vortex effects, the subcooled liquid washed the wick surface from both sides of the compensation chamber and became warmer after reflecting and converging upward at the evaporator center by adsorbing heat leakage from the shell and wick surface. While entering the wick, the fluid maintained a downward trend and diffused from both sides of the rib into the vapor channels. The liquid–vapor interface was basically located at the root of the rib structure, and the liquid–vapor interface at each rib expanded slightly inward because of the thermal paths created by the ribs. In addition, the vortex effects also affected the liquid–vapor interface in wick. Specifically, the liquid–vapor interface at wick center expanded more deeply for less cold liquid entering the wick. Also, the heat leakage at the places where the wick contacted the evaporator shell would heat liquid nearby and cause the liquid–vapor interface to expand more deeply than elsewhere.

Fig. 16 (a), (b), and (c) depict the temperature distributions at three different Z-direction cross section areas of the evaporator, namely the heater surface, rib contact surface, and wick surface on the compensation chamber side. Temperature on wick surface at the compensation chamber side showed an uneven but symmetrical distribution in Fig. 16 (c), that is, the temperature on the evaporator outlet side was much lower than that on the evaporator inlet side. As a result of the unequal

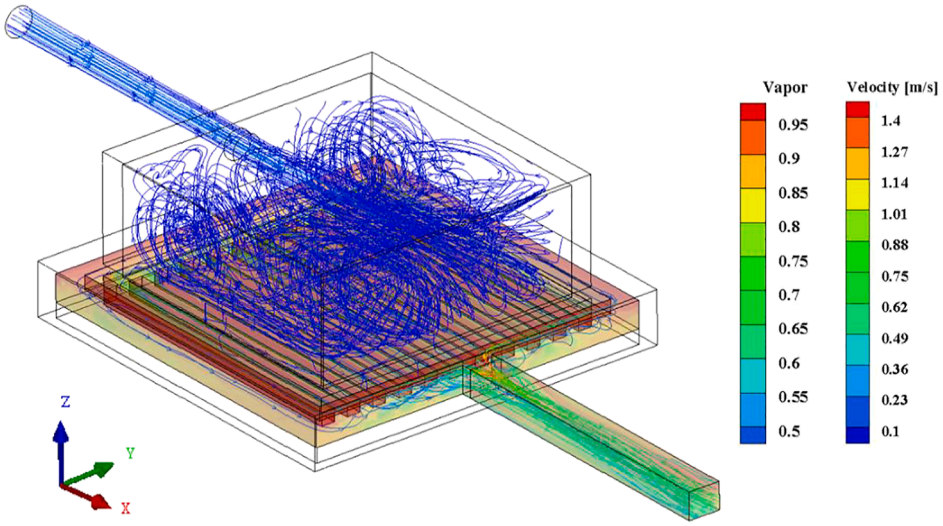

Fig. 14. Vapor phase distribution and streamline diagram at Q = 120 W and T_{sink} = 0 °C.

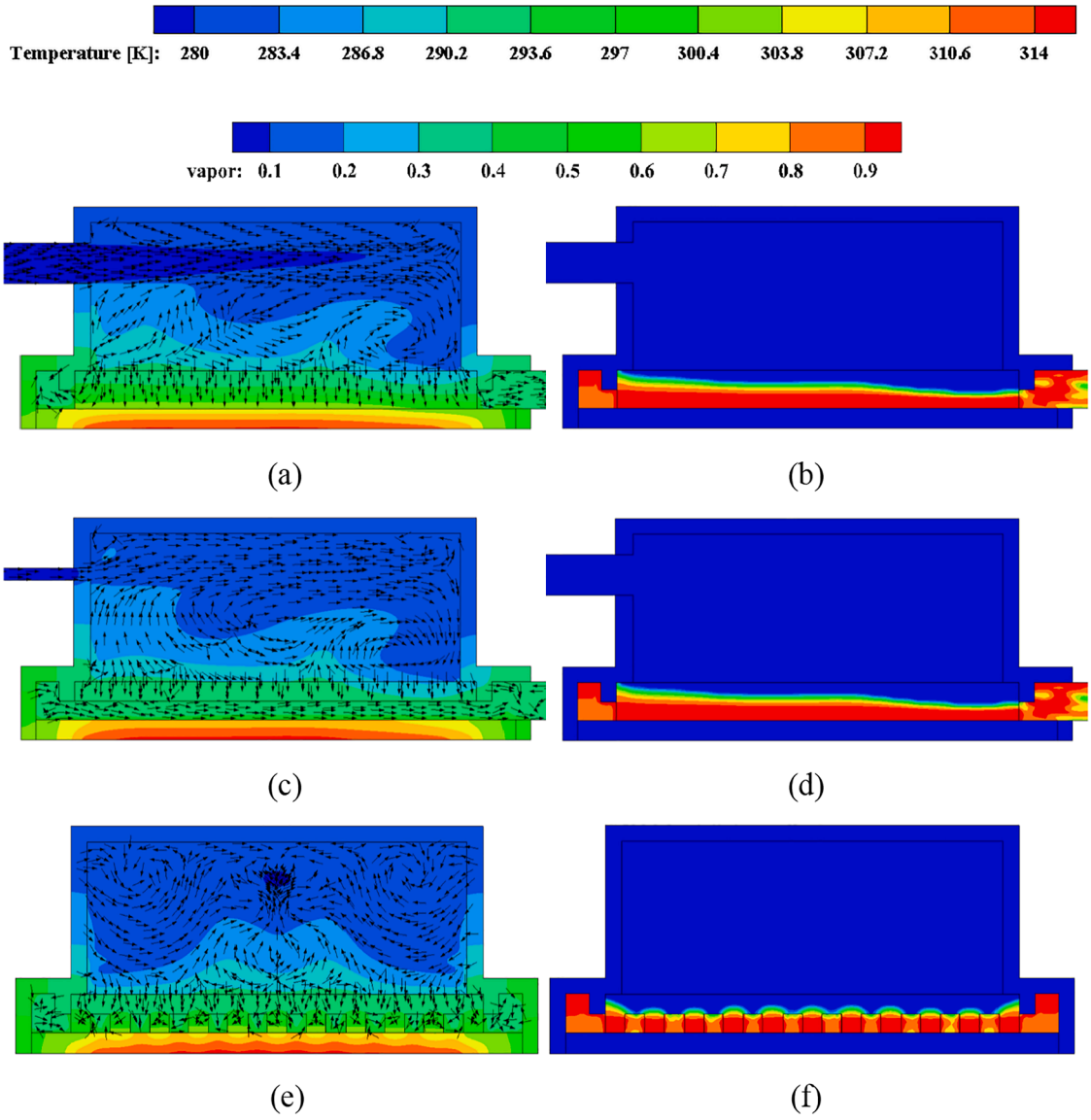

Fig. 15. Temperature, streamline, and vapor phase distribution diagrams at Q = 120 W and T_{sink} = 0 °C. (a)(b) Y-direction central cross sections at rib area. (c)(d) Y-direction cross sections at vapor channel area. (e)(f) X-direction central cross sections.

wetting intensity on wick surface caused by different scouring sequences and subcooled degrees of fluid, warmer subcooled liquid penetrated the wick on the left side, leading to an inclination of high-temperature zone to the left side as a whole. As shown in Fig. 16 (a), the heater surface temperature also exhibited a slightly uneven distribution by the above influence and the high temperature zone offset to the left side as well. Besides, it could be seen from Fig. 16 (b) that the places where ribs were contacted could introduce the heat into the wick interior better. Thermal transport in other places where the vapor channels and chamber existed were impeded by the thick vapor layer. Therefore, the places covered with ribs were much colder than other places covered with the vapor layer, forming a small temperature discrepancy between those places mentioned above.

5.3. *Effect of operating parameters*

The data analysis of the calculation results can provide specific insights into the operating parameter variation at each evaporator component. Fig. 17 (a), (b), and (c) present the variation trends of the volume average temperature, vapor volume percentage, and heat distribution percentage versus heat load at a heat sink temperature of 0 °C. Comparing Fig. 17 (a) with Fig. 6, under the same heat sink temperature condition, except for the maximum heat load condition where the wick suffered a dry-out situation, the variation trends of volume average temperatures at each evaporator component were consistent with the variation trends of characteristic temperatures in experiment. As the heat load increased, the mass flow rate in evaporator inlet was enlarged and more liquid with a lower subcooled degree was supplied to the liquid–vapor interface in wick, removing more heat from the heater surface. Therefore, the volume average temperature of the evaporator except for the heater surface reduced and reached a stable value accordingly, and the vapor volume percentage in wick reduced as well. The replenishment of sufficient subcooled liquid from the evaporator inlet was also continuous due to the steady velocity inlet boundary condition, hence no increase in the vapor volume percentage of the compensation chamber was observed in Fig. 17 (b). Subcooled liquid was filled inside the compensation chamber and the vapor volume percentage in the vapor collector was consistently above 80 %. However, the dry-out state that appeared in the experimental tests was caused by vapor leakage to the compensation chamber, meaning that the vapor phase was formed inside. Above which indicated that the calculation model could not imitate the actual situation of the maximum heat

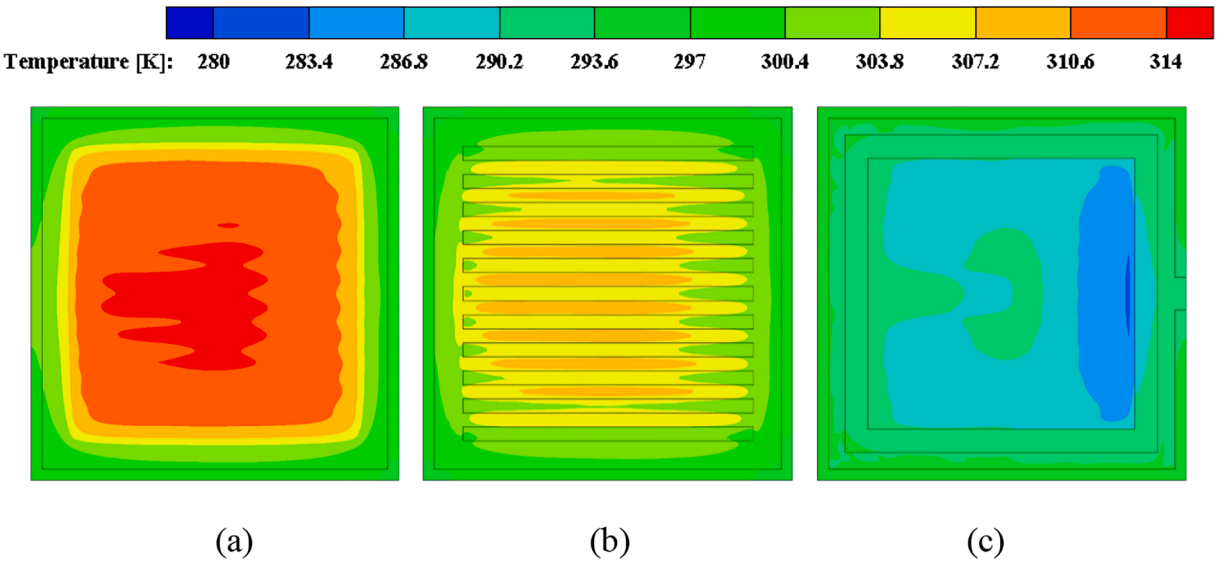

Fig. 16. Temperature distribution diagrams at Q = 120 W and T_{sink} = 0 °C. (a) Z-direction cross section at heater surface. (b) Z-direction cross section at rib contact surface. (c) Z-direction cross section at wick surface on compensation chamber side.

load where the wick suffered a dry-out state and the capillary force was insufficient. In addition, heat load distribution in Fig. 17 (c) illustrated that the heat conducted to the wick through the rib structure accounted for 84 % of the entire heat load, while the heat taken away by the vapor flow inside the vapor channels and collector accounted for 10 %, and the remaining 6 % was taken away by the compensation chamber and the ambient. This meant that most of the heat load was directly removed by the evaporation of the working fluid at the liquid–vapor interface. As the heat load increased, the sum of the heat adsorbed by the sensible heat of vapor in vapor channels and subcooled liquid in compensation chamber slightly increased, and the heat adsorbed by the latent heat of fluid correspondingly reduced. Furthermore, the heat transferred to the ambient accounted for the minimum portion and could be neglected accordingly.

Fig. 18 (a) and (b) present the effect of different heat loads and heat sink temperatures on vapor volume and heat distribution percentage of the flat-plate evaporator. It was apparent that the variation of heat sink temperature did a slight effect on vapor volume and heat distribution, and it would not affect the variation law of the vapor volume and heat distribution percentage versus heat load as well. The percentage of the vapor volume and heat distribution at each heat load condition was nearly the same except for the random discrepancy. The vapor volume in wick remained a reduced trend while increasing the heat load, and the amount of heat conducted to the wick was always more than that of taken away in vapor channels and compensation chamber.

5.4. Experimental comparison

Experimental comparison was conducted by comparing the simulation results with the experimental results to verify the veracity of the 3-D CFD calculation model. Fig. 19 presents the heater surface temperature comparison at various heat loads and heat sink temperatures. The temperature discrepancy of heater surface between the simulation and experimental results is calculated as follows,

$$\varepsilon_{HS} = \frac{\left|T_{cal\_HS} - T_{exp\_evap\text{-}in}\right|}{\left|T_{exp\_HS} - T_{exp\_evap\text{-}in}\right|} \tag{23}$$

Except for the maximum heat load condition, the simulation results followed the experimental results well, and the heater surface temperature continued to increase with the rise of heat load. Besides, different heat sink temperatures exhibited the same pattern that the discrepancy at the maximum heat load condition became much larger due to the dry-out state of the capillary wick. The calculation model was no longer suitable for reconstructing the actual situation in the experiment wherein the vapor leakage occurred. For other heat load working conditions, data analysis indicated that the maximum discrepancy of the heater surface temperature was 8.14 % at a heat load of 10 W, representing that the calculation model had a high accuracy and could precisely forecast the heater surface temperature even at different heat sink temperature and heat load conditions.

Fig. 20 presents the evaporator outlet temperature comparison at various heat loads and heat sink temperatures, verifying the accuracy of the calculation model from another perspective. The temperature discrepancy of the evaporator outlet between simulation and experimental results is calculated as follows,

$$\varepsilon_{evap\text{-}out} = \frac{\left|T_{cal\_evap\text{-}out} - T_{exp\_evap\text{-}in}\right|}{\left|T_{\exp\_evap\text{-}out} - T_{exp\_evap\text{-}in}\right|} \tag{24}$$

Apparently, the temperature tendencies were the same as those of the experimental values for the three heat sink temperature conditions. The temperature discrepancies were small and the results followed well except for the maximum heat load conditions. The simulation without a dry-out state could also lead to a misestimate of the vapor collector working situation, wherein the subcooled liquid infiltrating the wick was much colder than that of the experimental result. Thus, the calculation value of the evaporator heater surface was lower than that of the experiment value. With the exception of the maximum heat load conditions, the maximum discrepancy in evaporator outlet temperature was 10.29 % at a heat load of 160 W.

6. Conclusions

In this paper, a comprehensive study of a flat-plate evaporator LHP system from the perspective of experiment and numerical simulation is presented. First, a flat-plate evaporator LHP with the vapor leakage problem solved was fabricated and tested using a two-component epoxy resin adhesive to fill the assembly clearance. With the help of the experimental results and the VOF method, an effective 3-D CFD computational model, which could be utilized for future optimization studies in structure and design parameters, was proposed to simulate the flat-plate evaporator. Additionally, the mass flow rate of the loop was deduced from the heat leak effect in liquid line. The heat and mass

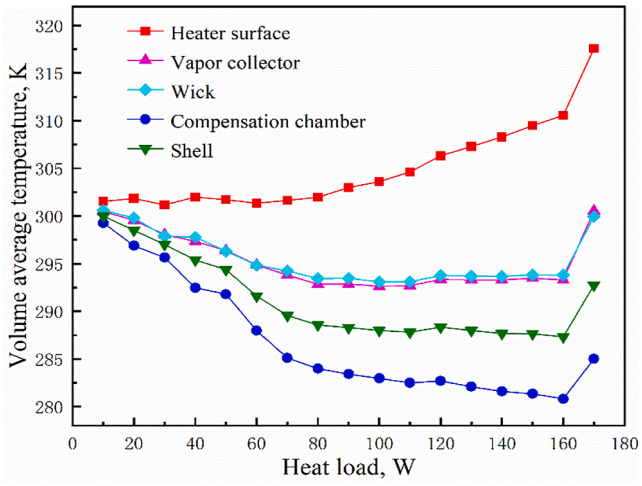

(a)

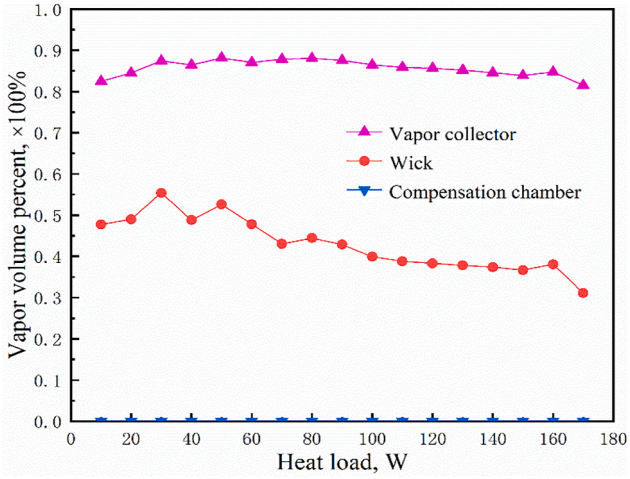

(b)

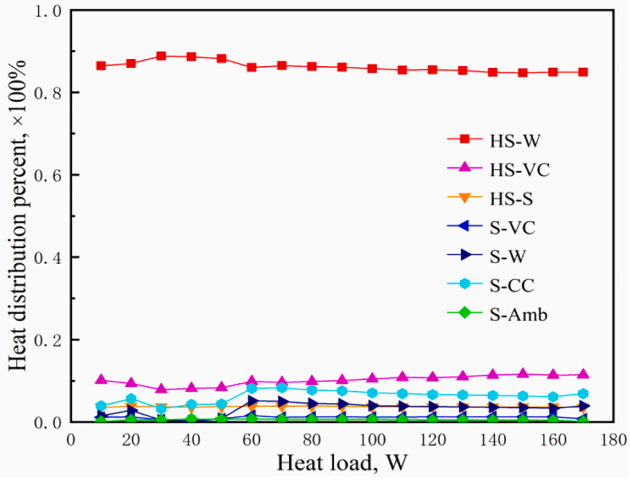

(c)

Fig. 17. Operating parameters versus heat load at T_{sink} = 0 °C. (a) Volume average temperatures of the evaporator components. (b) Vapor volume percentage at each fluid domain. (c) Heat distribution percentage between each evaporator component.

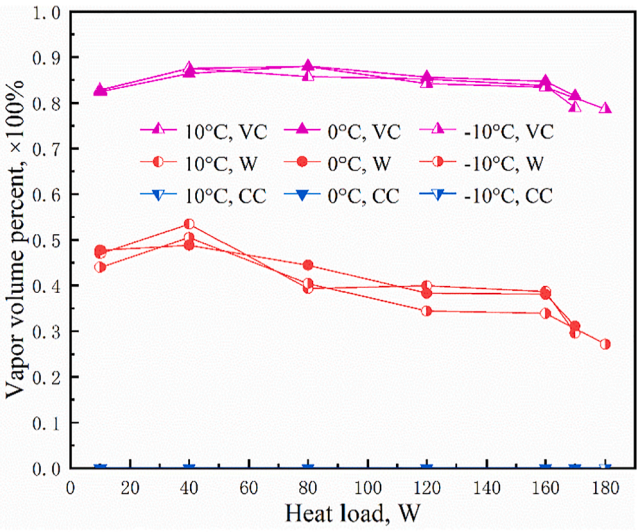

(a)

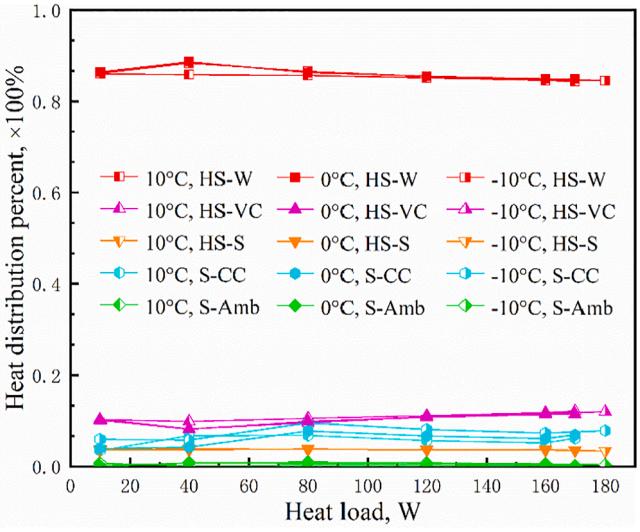

Fig. 18. Operating parameters versus heat load and heat sink temperature. (a) Vapor volume percentage at each fluid domain. (b) Heat distribution percentage between each evaporator component.

transfer performances, including flow regime, vapor phase, temperature, and heat distribution, were studied in detail. The main conclusions were summarized as follows.

1. The start-up and variable heat load tests illustrated that the maximum allowable heat load was up to 180 W (heat flux 11.25 W/cm^2) at a heat sink temperature of − 10 °C, and no temperature oscillation or even working failure was found for all operating conditions. Overall, the evaporator thermal resistance ranged from 0.1340 to 0.2137 °C/W.

2. The blockage of vapor leakage by the epoxy glue could significantly improve the thermal performance by reducing the operating pressure and enhancing the capillary performance. For the maximum heat load condition, a dry-out working state was formed in wick, and thus a severe temperature rise in heater surface occurred. Besides, the temperature hysteresis phenomenon attributed to the long liquid line occurred at the heater surface during the variable heat load tests.

3. The fluid scouring sequence inside the compensation chamber resulted in the generation of four symmetric vortices, causing uneven wetting on wick surface. The evaporation interface altered accordingly, and the high-temperature zone on heater surface offset to the evaporator inlet side. After turning into vapor, the fluid maintained a downward

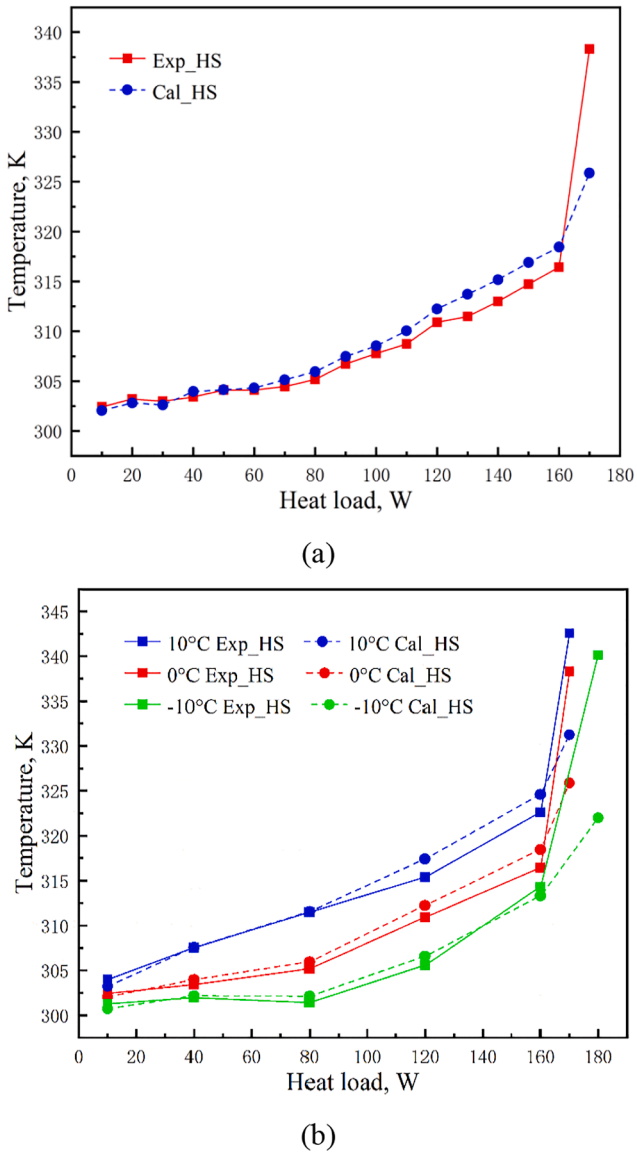

Fig. 19. Heater surface temperature comparison between simulation and experimental results. (a) Different heat loads at T_{sink} = 0 °C. (b) Different heat loads and heat sink temperatures.

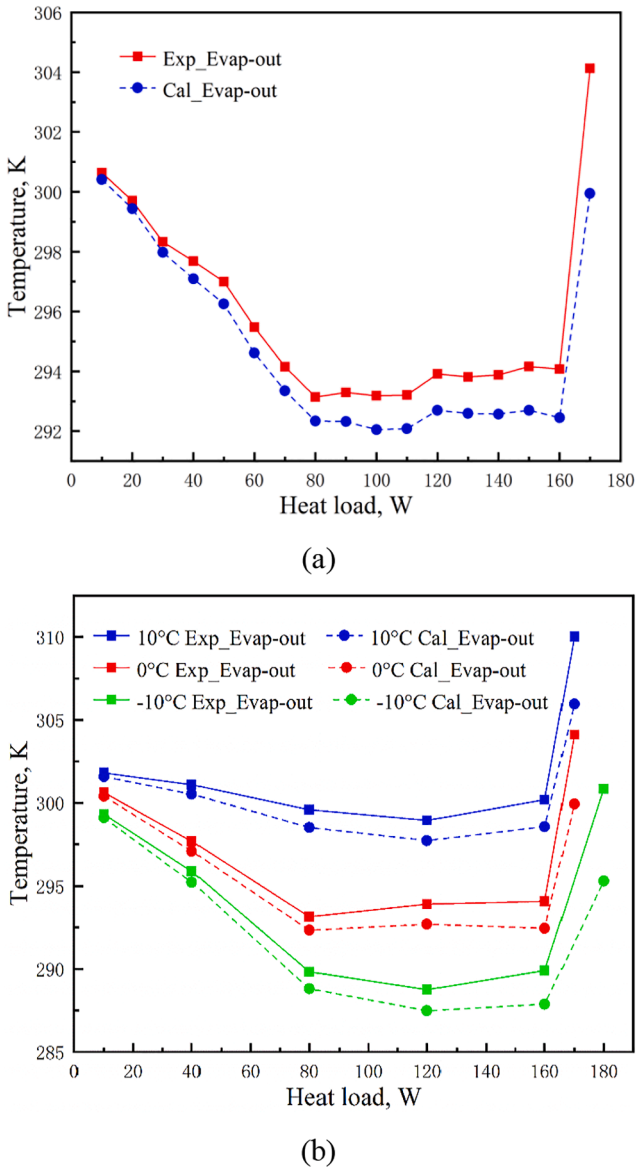

Fig. 20. Evaporator outlet temperature comparison between simulation and experimental results. (a) Different heat loads at T_{sink} = 0 °C. (b) Different heat loads and heat sink temperatures.

trend and diffused from both sides of the rib to the vapor channels, the vapor collector, and eventually to the evaporator outlet.

4. The thermal paths created by the ribs could quickly conduct heat from heater surface to wick. Thus, the liquid–vapor interface at each rib expanded slightly inward, and this part of the heat accounted for 84 % of the heat load on heater surface. The percentage of vapor volume and heat adsorbed during evaporation in wick changed oppositely to the heat load, and the heat sink temperature variation had no effect on the vapor volume or heat distribution percentage at the entire heat load range.

5. The mass flow rate deduced by the temperature discrepancy of the liquid line was positively linear with the heat load and independent of the heat sink temperature, which ranged between 9.45×10^{-5} and 0.001086 kg/s. Experimental comparison indicated that the calculation model had a high accuracy with the temperature discrepancies of heater surface and evaporator outlet less than 8.14 and 10.29 %, respectively.

Declaration of Competing Interest

The authors declare that they have no known competing financial interests or personal relationships that could have appeared to influence the work reported in this paper.

Data availability

No data was used for the research described in the article.

Acknowledgements

This study was supported by the National Natural Science Foundation of China (Nos. 51736004 and 52076088).

References

[1] Y.F. Maydanik, M. Chernysheva, V. Pastukhov, Loop heat pipes with flat evaporators, Appl. Therm. Eng. 67 (2014) 294–307.
[2] R.R. Riehl, Heat pipes and loop heat pipes acceptance tests for satellites applications, in: AIP Conference Proceedings, Vol. 1103, American Institute of Physics, 2009, pp. 82-90.

[3] T. Gao, T. Yang, S.-l. Zhao, Q.-l. Meng, The Design and Application of Temperature Control Loop Heat Pipe for Space CCD Camera, in: International Symposium of Space Optical Instrument and Application, Springer, 2017, pp. 65-74.
[4] J. Hartenstine, K. Walker, W. Anderson, Passive control of a loop heat pipe with thermal control valve for Lunar Lander application, in: 42nd International Conference on Environmental Systems, 2012, pp. 3542.
[5] F. Bodendieck, R. Schlitt, O. Brand, D. Labuhn, K. Goncharov, V.K.O. Golovin, Emerging Loop Heat Pipe Applications for Small-Sat, Mars Mission and ISS, in, SAE Technical Paper (2002).
[6] T. Shioga, Y. Mizuno, H. Nagano, Operating characteristics of a new ultra-thin loop heat pipe, Int. J. Heat Mass Transf. 151 (2020), 119436.
[7] Y.F. Maydanik, S.V. Vershinin, V.G. Pastukhov, S.S. Fried, Loop heat pipes for cooling systems of servers, IEEE Trans. Compon. Packag. Technol. 33 (2010) 416–423.
[8] F. Zhou, C. Li, W. Zhu, J. Zhou, G. Ma, Z. Liu, Energy-saving analysis of a case data center with a pump-driven loop heat pipe system in different climate regions in China, Energ. Buildings 169 (2018) 295–304.
[9] M. Bernagozzi, S. Charmer, A. Georgoulas, I. Malavasi, N. Michi, M. Marengo, Lumped parameter network simulation of a Loop Heat Pipe for energy management systems in full electric vehicles, Applied Thermal Engineering, 141 (2018) 617-629.
[10] R. Singh, T. Nguyen, Loop Heat Pipes for Thermal Management of Electric Vehicles, J. Therm. Sci. Eng. Appl. 14 (2021), 061010.
[11] S.-C. Wu, D. Wang, W.-J. Lin, Y.-M. Chen, Investigating the effect of powder-mixing parameter in biporous wick manufacturing on enhancement of loop heat pipe performance, Int. J. Heat Mass Transf. 89 (2015) 460–467.
[12] P. Gunnasegaran, M. Abdullah, M. Yusoff, Effect of Al2O3-H2O nanofluid concentration on heat transfer in a loop heat pipe, Procedia, Mater. Sci. 5 (2014) 137–146.
[13] Y. Maydanik, S. Vershinin, M. Chernysheva, The results of comparative analysis and tests of ammonia loop heat pipes with cylindrical and flat evaporators, Appl. Therm. Eng. 144 (2018) 479–487.
[14] R. Singh, A. Akbarzadeh, M. Mochizuki, Effect of wick characteristics on the thermal performance of the miniature loop heat pipe, J. Heat Transfer 131 (2009), 082601.
[15] X. Wang, J. Wei, Y. Deng, Z. Wu, B. Sundn, Enhancement of loop heat pipe performance with the application of micro/nano hybrid structures, International Journal of Heat and Mass Transfer, 127 (2018) 1248-1263.
[16] K. Fukushima, H. Nagano, New evaporator structure for micro loop heat pipes, Int. J. Heat Mass Transf. 106 (2017) 1327–1334.
[17] B. Weisenseel, P. Greil, T. Fey, Biomorphous silicon carbide as novel loop heat pipe wicks, Adv. Eng. Mater. 19 (2017) 1600379.
[18] B.-J. Huang, Y.-H. Chuang, P.-E. Yang, Low-cost manufacturing of loop heat pipe for commercial applications, Appl. Therm. Eng. 126 (2017) 1091–1097.
[19] S. He, P. Zhou, Z. Ma, W. Deng, H. Zhang, Z. Chi, W. Liu, Z. Liu, Experimental study on transient performance of the loop heat pipe with a pouring porous wick, Appl. Therm. Eng. 164 (2020), 114450.
[20] B. Furst, S. Cappucci, T. Daimaru, E. Sunada, S. Roberts, T., O'Donnell, An Additively Manufactured Evaporator with Integrated Porous Structures for Two-Phase Thermal Control, in. 48th International Conference on Environmental Systems, 2018.
[21] N. Watanabe, N. Phan, Y. Saito, S. Hayashi, N. Katayama, H. Nagano, Operating characteristics of an anti-gravity loop heat pipe with a flat evaporator that has the capability of a loop thermosyphon, Energ. Conver. Manage. 205 (2020), 112431.
[22] N.S. Ramasamy, P. Kumar, B. Wangaskar, S. Khandekar, Y.F. Maydanik, Miniature ammonia loop heat pipe for terrestrial applications: Experiments and modeling, Int. J. Therm. Sci. 124 (2018) 263–278.
[23] L. Bai, G. Lin, D. Wen, Modeling and analysis of startup of a loop heat pipe, Appl. Therm. Eng. 30 (2010) 2778–2787.
[24] E.G. Jung, J.H. Boo, A Novel Analytical Modeling of a Loop Heat Pipe Employing the Thin-Film Theory: Part I-Modeling and Simulation, Energies 12 (2019) 2408.
[25] M. Nishikawara, H. Nagano, M. Prat, Numerical study on heat-transfer characteristics of loop heat pipe evaporator using three-dimensional pore network model, Appl. Therm. Eng. 126 (2017) 1098–1106.
[26] M.A. Chernysheva, V.G. Pastukhov, Y.F. Maydanik, Analysis of heat exchange in the compensation chamber of a loop heat pipe, Energy 55 (2013) 253–262.
[27] Y. Zhang, J. Liu, L. Liu, H. Jiang, T. Luan, Numerical simulation and analysis of heat leakage reduction in loop heat pipe with carbon fiber capillary wick, Int. J. Therm. Sci. 146 (2019), 106100.
[28] J. Li, G.P. Peterson, 3D heat transfer analysis in a loop heat pipe evaporator with a fully saturated wick, Int. J. Heat Mass Transf. 54 (2011) 564–574.
[29] L. Mottet, M. Prat, Numerical simulation of heat and mass transfer in bidispersed capillary structures: application to the evaporator of a loop heat pipe, Appl. Therm. Eng. 102 (2016) 770–784.
[30] J. Li, F. Hong, R. Xie, P. Cheng, Pore scale simulation of evaporation in a porous wick of a loop heat pipe flat evaporator using Lattice Boltzmann method, Int. Commun. Heat Mass Transfer 102 (2019) 22–33.
[31] B. Chen, W. Liu, Z. Liu, H. Li, J. Yang, Experimental investigation of loop heat pipe with flat evaporator using biporous wick, Appl. Therm. Eng. 42 (2012) 34–40.
[32] Z. Zhang, H. Zhang, Z. Ma, Z. Liu, W. Liu, Experimental study of heat transfer capacity for loop heat pipe with flat disk evaporator, Appl. Therm. Eng. 173 (2020), 115183.
[33] W.H. Lee, A pressure iteration scheme for two-phase modeling, Los Alamos Scientific Laboratory, Los Alamos, NM, Report No, LA-UR (1979) 79–975.
[34] J.D. Anderson, J. Wendt, Computational fluid dynamics, Springer, 1995.
[35] M. Knudsen, Maximum rate of vaporization of mercury, Annalen der Physik 47 (1915) 697–705.
[36] H. Hertz, On the evaporation of liquids, especially mercury, in vacuo, Annalen der Physik 17 (1882) 178–193.
[37] A. Fluent, Ansys fluent theory guide, Ansys Inc, USA 15317 (2011) 724–746.
[38] J.U. Brackbill, D.B. Kothe, C. Zemach, A continuum method for modeling surface tension, Journal of Computational Physics, 100 (1992) 335-354 %@ 0021-9991.
[39] S. Ergun, Fluid flow through packed columns, Chem. Eng. Prog. 48 (1952) 89–94.
[40] M. Kaviany, Principles of heat transfer in porous media, Springer Science & Business Media, 2012.